Characterizing Nanoscale Precipitation in a Titanium Alloy by Laser-Assisted Atom Probe Tomography

James Coakley*[1,2], Anna Radecka[3,4], David Dye[3], Paul A.J. Bagot[5], Tomas L. Martin[5], Ty J. Prosa[6], Yimeng Chen[6], Howard J. Stone[2], David N. Seidman[1,7,8], Dieter Isheim[1,7]

[1]Northwestern University, Department of Materials Science and Engineering, Evanston, IL 60208-3108, USA.
[2]Department of Materials Science and Metallurgy, University of Cambridge, Cambridge CB3 0FS, England.
[3]Department of Materials, Imperial College, South Kensington, London SW7 2AZ, England.
[4]Rolls Royce Plc., Elton Road, Derby DE24 8BJ, England.
[5]Department of Materials, University of Oxford, Oxford OX1 3PH, England.
[6]CAMECA Instruments Inc., Madison, WI 53711, USA.
[7]Northwestern University Center for Atom-Probe Tomography (NUCAPT); 2220 Campus Drive; Evanston, Illinois, 60208, USA.
[8]NanoAl LLC, 8025 Lamon Ave, Skokie, IL 60077, USA.

*E-mail: james.coakley@northwestern.edu Phone: +1-312-774-8634 Fax: +1-847-467-2269

Abstract

Atom-probe tomography was performed on the metastable β-Ti alloy, Ti-5Al-5Mo-5V-3Cr wt.% (Ti-5553), aged at 300 °C for 0 to 8 h, to precipitate the embrittling isothermal ω phase. Accurate precipitate quantification requires monitoring and controlling suitable charge-state ratios in the mass spectrum, which in turn are closely related to the laser pulse energy used. High ultraviolet laser pulse energies result in significant complex molecular ion formation during field-evaporation, causing mass spectral peak overlaps that inherently complicate data analyses. Observations and accurate quantification of the ω-phase under such conditions are difficult. The effect is minimized or eliminated by using smaller laser pulse energies. With a small laser pulse energy, Ti-rich and solute depleted precipitates of the isothermal ω phase with an oxygen enriched interface are observed as early as after 1 h aging time utilizing the LEAP 5000X S (77% detection efficiency). We note that these precipitates were not detected below a 2 h aging time with the LEAP 4000X Si (58% detection efficiency). The results are compared to the archival literature. The Al concentration in the matrix/precipitate interfacial region increases during aging. Nucleation of the α-phase at longer aging times may be facilitated by the O and Al enrichment at the matrix/precipitate interface (both strong α-stabilisers). The kinetics and compositional trajectory of the ω-phase with aging time are quantified, facilitating direct correlation of the APT data to previously published mechanical testing.

Keywords

atom probe tomography, titanium alloys, ω-phase, precipitation, aging

Introduction

Near α-Ti alloys, α plus β-Ti alloys and metastable β-Ti alloys are susceptible to thermally induced phase-transformations, which dramatically alter their mechanical properties. The characterisation and quantification of these phases can be inherently difficult, particularly when the precipitates are small (<10 nm) relative to the thickness of a TEM foil or when the compositional contrast between the precipitate and matrix is small, making detection by atom-probe tomography (APT) challenging. Such limitations with characterization methods have hindered our understanding of α_2 formation in near-α and α plus β-Ti alloys, which is detrimental to fracture toughness and cold dwell fatigue resistance of components in gas-turbine engines [1-6]. It has also hindered our understanding of athermal ω (ω_a), which forms on quenching, and isothermal ω (ω_i), which forms on subsequent low-temperature aging of metastable β-Ti alloys [7-12]. The ω_a phase forms by a diffusionless transformation. The ω_i phase forms by subsequent diffusion during low-temperature aging at and below ~350 °C and therefore it possesses a different composition from that of the β-matrix. Typically, the ω-phase is undesirable as it embrittles the alloy [10]; it is, however, generally believed to be a precursor to the formation of stable nanoscale α-precipitates that highly strengthen the alloy [8, 9, 13, 14]. This precipitation sequence is not fully understood, and a vast amount of APT research has been published recently to help further our insight into the precipitation mechanisms of the high-strength-to-weight β-Ti alloys: Ti-5Al-5Mo-5V-3Cr wt.% (Ti-5553); and Ti-6Cr-5Mo-5V-4Al (wt.%) (Ti-6554) [9, 11-17].

Figure 1(a) illustrates the deleterious effects on mechanical properties associated with ω_i precipitation in 24 h aged Ti-24Nb-4Zr-8Sn wt.% (Ti-2448) [10]. The alloy became increasingly brittle and stiff with higher aging temperatures up to 250 ^{o}C. It is striking that an age of just 80 ^{o}C/24 h has such a profound effect on mechanical properties. Identifying such early stage precipitation of ω_i from ω_a by TEM is inherently complicated. The associated diffraction spots are weak and diffuse and diffraction spot brightness is dependent on foil-thickness. Such weak diffraction also complicates dark-field imaging. In the study of Ti-2448 the embrittlement following the 80 ^{o}C/24 h treatment could only be associated with ω_i formation from the trend in the mechanical data and observing ω_i formation in the 250 ^{o}C/24 h aged sample. Figure 1(b) shows an increase in Vickers hardness of Ti-5553 after a 300 ^{o}C/1 h aging treatment, associated with ω_i formation [10]. Previously, these precipitates were not identified in this heat-treatment by APT analyses utilizing a LEAP 4000X Si [11] but were observed by TEM and small-angle neutron-scattering (SANS) [10]. This introduction highlights that advancement in materials characterization techniques is required to characterize the earliest stages of nanoprecipitation, which can alter dramatically the mechanical properties.

The ongoing development of commercially available local-electrode atom-probe (LEAP) tomographs has recently permitted unparalleled compositional analyses of nanoscale precipitates in Ti-alloys. Characterization of the ω-phase in Ti-5553 and Ti-6554 alloy has been attempted with voltage pulsing [13, 18] and laser pulsing [9, 11,14,15,17]. Because ω–phase containing Ti-alloys are brittle, laser pulsing can assist in achieving more

data per APT experiment prior to specimen fracture. The laser pulse energy can induce undesirable thermal effects, such as surface diffusion or the formation of complex molecular ions. The thermal effects make data analyses more difficult and can obscure second phase precipitates, possibly influencing data regarding ω-phase found in the literature. There are clear differences in the results obtained regarding the ω-phase in β-Ti alloys, specifically focusing on Ti-5553 and Ti-6554. The first APT measurements of Ti-5553 with a 2 h aging treatment at 350 °C identified the ω–precipitates as a phase with very similar composition to that of the β– matrix [18]. More recently, the same authors demonstrated that slow heating at 5 °C /min to 350 °C (a 70 min aging treatment) resulted in ω-phase precipitates, which are depleted in all solute additions [13]. This is in agreement with our current observations. Finally, it has also recently been reported that the ω-phase in Ti-6554 aged at 300 °C for 0 to 8 h is a Mo-depleted precipitate, with all the other solute additions equal to their bulk concentrations [14,17]. Such results are of significance as they are used to rationalize the precipitation sequence of $\beta \rightarrow \beta + \omega_a \rightarrow \beta + \omega_i \rightarrow \beta + \alpha$. Thus, a study of the characterization of the ω-phase in β-Ti alloys by APT is timely and warranted.

This article demonstrates potential characterization errors, which can arise when the laser pulse energy is too high. It also notes a case where early stage precipitation is detected and characterized by the LEAP 5000X S and *not* the LEAP 4000X Si, which suggests that there may also be an instrumental dependence. Our results do not identify athermal ω-formation at Mo depleted zones in Ti-5553, in agreement with SANS measurements of the same alloy [9]. The titanium-rich and solute-depleted isothermal ω-phase is identified as early as after 1 h aging at 300 °C, in agreement with [13]. Finally, the evolution of the isothermal ω-phase between 0 and 8 h aged at 300 °C is quantified herein.

Materials and Methods

Materials and Methods: Sample Preparation

The forged billet of Ti-5553 used in this research has previously been studied and described [9,19]. All samples were prepared by initially heat-treating Ti-5553 at 900 °C for 30 min, followed by water quenching. Four samples were subsequently aged at 300 °C for 1, 2, 4, and 8 h and finally air-cooled. These aging conditions complement previously published studies of Ti-5553 by small-angle neutron-scattering (SANS), transmission electron microscopy (TEM), micro-hardness measurements and APT [9,11]. All heat-treatments were performed with the samples encapsulated within an argon atmosphere.

Following heat-treatment, APT samples of the quenched condition and aged conditions were prepared using a standard lift-out, nanotip mounting, and nanotip sharpening method [20] employing an FEI Helios NanoLab 600 Dual-Beam focused ion-beam (FIB) microscope equipped with an Omniprobe Autoprobe 200 micromanipulator. Additional aspects of the FIB lift-out procedure can be found elsewhere, for example [21].

Materials and Methods: APT Data Acquisition & Test Matrix

All APT experiments were performed with laser pulsing on Cameca's LEAP instruments, representing four different models and configurations at different research facilities. The

full test matrix is displayed in Table 1, which was designed to examine the dependence of precipitate identification and quantification with laser pulse energy and with the relative intensities of the peaks for different charge states (the so-called *charge-state* ratios (CSR)).

The HR tomographs have an energy-compensating reflectron lens that improves mass resolution mostly in voltage mode and reduces background noise to some degree, albeit with decreased detection efficiency. The Si and S tomographs have a straight flight-path with higher detection efficiency. The detection efficiency of the reflectron instruments (LEAP 3000X HR and LEAP 4000X HR) is ~37 %, while the LEAP 4000X Si and LEAP 5000 XS straight flight-path instruments have ~58 and ~77 % detection efficiency, respectively [22,23]. The LEAP 3000X HR is equipped with a green laser, λ = 532 nm and is marked by an asterix* in Table 1, while all other tomographs in this work are equipped with a UV picosecond laser, λ = 355 nm. The laser pulse energies and specimen stage temperatures used for each measurement are listed along with the specific tomograph, ion detection efficiency, total ion counts of each measurement run in millions (M) detected, and whether precipitates were identified by APT (Y) or not (N). The combination of the APT measurements provide accurate quantitative evaluation of the ω-phase evolution during isothermal aging at 300 °C for aging times ranging from 0 to 8 h.

A 300 °C/8 h aged APT specimen was measured with an initial 30 pJ laser pulse energy. The laser pulse energy was then decreased to collect data at 10 pJ, in order to investigate the dependence between these energies, the charge-state ratios, and precipitate characterization. Similarly, a 300 °C/ 2 h APT specimen was measured with an initial 30 pJ laser pulse energy, then increased for measurements at 40 pJ and finally at 50 pJ, Table 1. Both these experiments were performed on a LEAP 4000X Si.

The 300 °C/8 h aged APT specimens were measured on the LEAP 3000X HR at Oxford University, the LEAP 4000X HR at Harvard University, and the LEAP 4000X Si at Northwestern University. Quenched samples and 300 °C /1 h aged samples were measured on the LEAP 4000X Si at Northwestern University and LEAP 5000X S at CAMECA instruments, Table 1.

Materials and Methods: APT Data Reconstruction & Analysis

After data collection, runs were reconstructed and examined in three-dimensions (3-D) utilising CAMECA's IVAS data analysis software program, version 3.6.12.

The detection efficiency for the various APT systems used in this work together with the known shape of the precipiates was used to obtain a correct atomic density and the correct equiaxed shape of the precipitates in the reconstruction. The mass-to-charge-state ratio (*m/z*) binning size of all the mass spectra was 0.01. The mass spectra were analysed carefully to assign correctly the isotopic elemental or molecular identity and to detect potential mass spectral peak overlaps, specifically between $(TiH)^+$ and Mo^{2+} ions, in addition to the known direct mass spectral peak overlaps of isotopes of different elements, such as $^{50}Ti^+$ and $^{50}Cr^+$, or $^{100}Mo^{2+}$ and $^{50}Cr^+$. The criterion for ranging each mass spectral peak was defined at 10% of the peak intensity. 10^o specimen shank angles were defined in order to obtain continuous reconstructions, approximated from SEM imaging. The presence of Ti-rich ω-precipitates was identified with a combination of statistical methods and real-space visualization.

Firstly, Ti concentration frequency distribution functions were calculated to verify whether statistically significant deviations from a binomial distribution were present on a scale relevant to nanometer-sized precipitates [24]. The binomial distribution represents a random solid-solution distribution of an alloy with the same mean composition. Block sizes varying between N=100 and N=250 atoms were calculated using the IVAS program, corresponding to sampling volumes between approximately 3.5 and 8.8 nm^3.

Secondly, Ti isoconcentration surfaces were used to identify and visualize the statistically significant Ti-rich ω–regions. Thirdly, proximity histogram concentration profiles (proxigrams) [25-30] were then created relative to the Ti isoconcentration-surfaces for quantitative compositional analysis of the ω–precipitates. Phase compositions were measured from the plateau regions in the proxigrams. In an iterative approach, the average Ti-concentration between the Ti-rich ω-phase and Ti-depleted beta-phase was then used for establishing a refined isoconcentration surface threshold and proxigram concentration profile analysis. Table 1 presents the total ion counts acquired in each APT measurement run for the different aging times as well as a designation of whether Ti-rich precipitates were identified for each experimental run or not. Table 2 presents the total ion counts used in each reconstruction.

Results

Results: Mass Spectra Analysis

The APT mass spectra obtained with different laser pulse energies of 10 and 30 pJ with the same nanotip are displayed in Figure 2. Figure 2(b) – (e) are enlarged sections of these mass spectra shown in Figure 2(a), to highlight individual peaks of isotope groups and their relative intensities for the elemental or molecular ions in question. Specifically, the mass spectral overlap of several Mo^{2+} isotopes and $(TiH)^+$ peaks in Figure 2(c), and of $(Mo_2)^{3+}$ and $(TiO)^+$ peaks in (d), and Mo^+ and $(Mo_2)^{2+}$ in 2(e) are highlighted. From Figure 2(c), the two mass spectra differ in their relative peak intensities. The higher laser pulse energy produced the formation of complex molecular $(TiH)^+$ ions, which overlap with the Mo^{2+} isotopic peaks at m/z = 47, 48, 49, and 50 Da. Additionally, the higher laser pulse energy promotes field-evaporation of singly-charged Cr and possibly V ions, creating additional overlaps of $(TiH)^+$ with $^{50}Cr^+$ at m/z = 50 Da and $^{51}V^+$ at m/z = 51 Da. As peaks are expected for Mo, V, and Cr in this region, the subtle changes of the relative peak intensities associated with $(TiH)^+$ can go undetected, and errors with concentration quantification can arise from these peak overlaps. These $(TiH)^+$ peaks were not immediately apparent and were only noticed on overlaying the 30 and 10 pJ mass spectra.

$(TiO)^+$ is also formed, overlapping $(Mo_2)^{3+}$ at m/z = 62, 63, 64, 65, and 66 Da, Figure 2(d). Complex molecular-ion formation is particularly apparent in Figure 2(e), where the 30 pJ laser pulse energy results in creation of $(Mo_2)^{2+}$. The $(Mo_2)^{2+}$ peaks overlap with Mo^+ peaks between m/z = 92 – 100 Da. The formation of $(Mo_2)^{2+}$ ions in laser-pulsed APT at higher laser pulse energies was previously noted for pure Mo [31,32] and for Ni-based superalloys [33]. The higher laser pulse energies produce a higher temperature at the nanotip surface at the time of field-evaporation, and these references [31-33] provide detailed analyses of the relative intensities of peaks for Mo^+ and $(Mo_2)^{2+}$.

Employing lower laser pulse energies reduces the probability of forming complex molecular ions. At higher laser pulse energies, the overlapping peaks make the processing of the mass spectra and quantification of compositions inherently more difficult for this alloy. The Mo^{2+} peaks at m/z = 46, 47.5, and 48.5 Da are unaffected by the isobaric overlap with $(TiH)^+$. Thus, quantitative concentrations of Mo can be determined by using the Mo^{2+} peaks at m/z = 46, 47.5, and 48.5 Da and calculating the correct number of Mo atoms using the tabulated natural abundances of the isotopes [34]. The correction process is, however, tedious. Conversely, the contribution of $(TiH)^+$ can be estimated by calculating the intensity of the $^{98}Mo^{2+}$ peak from the natural isotopic abundances of Mo and subtracting from them the intensity of the peak at m/z = 49 Da, representing 73.72% of $(TiH)^+$.

At lower laser pulse energies, the $(TiH)^+$ ions constitutes only a negligible fraction of the detected Ti atoms (< 1%). Their contribution may therefore be safely neglected while maintaining a relative error below 1%.

Results: Bulk Composition

The bulk compositions following mass spectra analysis are presented in Table 2, in at.%. The compositions presented have not been corrected for the previously described overlapping peaks, which are particularly prevalent at higher laser pulse energies. The apparent bulk concentration of Mo is seen to increase from 2.8 to 4.5 at.% when the laser pulse energy is increased from 30 to 50 pJ on a single specimen, highlighted in bold font in the table. The error is associated with an increase in complex molecular-ion formation at higher laser pulse energies, which has not been accounted for in the mass spectra analyses. This indicates that the probability of error in bulk concentrations deduced is increased at higher laser pulse energies. The relationship between the charge-state ratios and bulk compositions is analysed in the Discussion.

Results: APT Reconstructions and Concentration Frequency Distribution Analysis

Figure 3(a) shows a 3-D APT reconstruction of Ti-5553 aged for 2 h at 300 °C. The data was collected on a LEAP 4000X Si aton-probe tomograph equipped with a UV laser, and the pulse energy was stepped from 30 to 40 and 50 pJ after ~15 million ions collected, respectively. Superposed is an 86 at.% Ti isoconcentration surface (red) to highlight the Ti-enriched regions. This isoconcentration surface value was applied to best visually illustrate the effect of increasing the laser pulse energy through the bulk of the needle. The 30 and 40 pJ reconstructions look quite similar. There is, however, a clear effect at 50 pJ with visually fewer and smaller Ti-enriched regions observed. There also appears to be more Mo ions (blue) in the 50 pJ section of the reconstruction. This is also noted in the apparent bulk concentration results, Table 2.

The uncorrected measured Ti-concentration frequency distribution functions for the sample aged for 2 h at 300 °C are displayed in Figure 3(b) – (d), measured with (b) 30, (c) 40, and (d) 50 pJ laser pulse energies. The subtle changes in elemental concentrations with increased laser pulse energy are evident from the shift of the mean Ti concentration (vertical dashed lines). The experimentally measured distribution is shifted toward lower Ti concentration-values for the higher laser pulse energies, Figure 3(b) to 3(d). This is related to the formation of complex molecular ions at higher laser pulse energies,

incorrectly being identified as Mo^{2+} ions in the mass spectra. The three concentration frequency distributions are significantly broader than their respective binomial functions, specifically with a lower maximum and with a significant tail on the Ti-rich side. The chi-squared statistic between frequency distribution functions and binomial functions is reduced from 48 (30 pJ, CSR=5.2, Figure 3b), to 32 (40 pJ, CSR=3.2, Figure 3c), to 20 (50 pJ, CSR=2.4 Figure 3d). Therefore, the correlation between Ti-concentration frequency distribution and the binomial function is lower at the lower laser-pulse energies i.e. element partitioning is statistically more prevalent at lower laser pulse energies. In all cases the P-value is <0.0001 with an alpha level = 0.01, confirming the differences between the frequency distribution functions and binomial distributions (Figures 3b – 3d) are statistically significant. The Ti-rich tails are indicative of the presence of Ti-rich regions associated with the isothermal ω-phase. The tails are most pronounced at lower laser pulse energies, Figure 3(b) versus 3(d), respectively. In practice, however, the laser pulse energy cannot be arbitrarily low as this results in a high dc field and a preferential loss of atoms that evaporate between laser pulses (so-called *dc-field evaporation*). Since the atoms evaporating between laser pulses increases the random noise in the mass spectrum, a lower limit for the laser pulse energy is established by ensuring that the background noise does not increase when decreasing the laser pulse energy.

Figure 4(a) shows the effect of decreasing the laser pulse energy from 30 to 10 pJ for an APT reconstruction of a sample aged for 8 h at 300 °C. The laser direction is highlighted, and an 88 at.% Ti isoconcentration surface is superposed (red) to highlight the Ti-enriched regions. This higher isoconcentration surface value is used as it visually highlights an inhomogeneity associated with the incident laser direction at high laser pulse energies. It illustrates the apparent Mo enrichment (blue)/depletion of Ti-rich regions (red) on the laser side of the nanotip at the 30 pJ laser pule energy setting, in this measurement. This effect is clearly minimized or eliminated entirely with the lower laser pulse energy at 10 pJ. Figure 4(b) and (c) show 40 nm thick slices of the 3-D reconstruction, obtained with a 30 pJ laser pulse energy and 10 pJ laser pulse energy, respectively. Figure 4(a) – (c) are shown on the same length scale and employ the same isoconcentration surface value of 88 at.% Ti. The apparent compositional inhomogeneity throughout the specimen, induced by the higher laser pulse energy is particularly apparent in Figure 4(b) when compared to Figure 4(c). The issues arising from complex molecular ion formation are inhomogeneous, with greater formation on the laser side of the nanotip than the shadow side.

Results: Quantifying the Initial Nucleation and Growth of the Isothermal ω Phase

It is known from SANS that ω_i precipitation occurs in under 1 h of aging at 300 °C in Ti-5553 [9]. However, characterization of initial ω_i nucleation by APT has proven elusive, and is now carefully revisited. Figures 5 (a) and (b) display 3-D APT reconstructions for the sample aged 1 h at 300 °C, collected on the LEAP4000X Si and 5000X S, respectively. Eighty-five at.% Ti isoconcentration surfaces are superposed to highlight Ti-rich regions. The significance of any Ti-enriched region is analyzed in Figures 5 (c) and (d) utilizing a Ti concentration frequency distribution, for the data collected on the LEAP4000X Si and 5000 XS, respectively. From the significant tail in the distribution obtained with the LEAP 5000X S, indicated by an arrow in Figure 5(d); Ti-rich precipitates are present. The frequency of

Ti-rich bins exceeds the random binomial reference distribution. From this distribution, the 85 at.% Ti isoconcentration threshold value is effective in identifying Ti-rich precipitates in the 3-D reconstruction displayed in Figures 5(b). There is no indication, however, of these precipitates from the Ti concentration frequency distribution obtained with the LEAP4000X Si, Figure 5(c). Thus from Figure 5, Ti-rich regions have been identified in a 300 ^{o}C/1 h aged sample measured by a LEAP 5000X Si but not in a sample measured utilizing a LEAP 4000X Si when using similar instrument parameters, Table 1. This is discussed further in the subsection titled *Discussion: Discrepancies in the Experimental Data.*

Compositional analysis of the Ti-rich precipitates is performed utilizing the proximity histogram concentration profile method. The proxigrams for samples aged 1 and 8 h at 300 °C are displayed in Figure 6(a) – (c), which were created from 85 at.% Ti isoconcentration surface values. The 1 h aged data was recorded on a LEAP 5000X S, and the 8 h data was recorded on a LEAP 4000X Si. The precipitates are Ti-rich relative to the β-matrix, Figure 6(a). They are depleted in all solute additions (Al, V, Cr, Mo, and Fe), Figure 6(b). We note that the precipitate/matrix interfacial region is rich in oxygen (O), Figure 6(c), commencing just after 1 h. Due to the low O concentration in the alloy, a large dataset is required to identify the peak at the interface with good counting statistics. For this reason, the peak is clear in the 1 h aging treatment dataset measured on the LEAP5000X S (46 million atoms, Table 2), but somewhat obscured in the error range of the 8 h aging treatment dataset measured employing the LEAP4000X Si (8 million atoms, Table 2). An O rich ω/β heterophase-interface has been noted elsewhere [11]. The precipitates and the interfacial region become richer in Al between the 1 h and 8 h aging treatments, Figure 6(b).

Eighty-five at.% Ti isoconcentration surfaces were used to quantify volume fraction, precipitate number density, and volume equivalent mean-radius of the ω precipitates, Figure 7(a), (b), and (c), respectively. The volume fraction was calculated by the ratio of all atoms contained within all precipitates to the total of atoms in each APT 3-D reconstruction. The number density of precipitates was calculated accounting for detector efficiency and assuming the β body-centered cubic (bcc) unit cell volume determined at room temperature for Ti-5553 [19]. This is a reasonable assumption due to the low volume fraction of precipitates. The equivalent spherical volume of each precipitate was calculated from the atom counts, correcting for detector efficiency, and assuming a hexagonal ω unit cell volume of pure Ti [35]. The volume-equivalent radius of each precipitate was calculated and the dependence of the mean volume-equivalent radius with aging time is plotted in Figure 7(c). Guides to the eye have been added to each plot under the assumption that the 10 pJ laser pulse energy data sets are consistently the most accurate measurements. Approximate error bars of 5% error are indicated for these microstructural parameters as an estimate, Figure 7(a)-(c). It is assumed that the error is dominated by the counting statistics of the number of precipitates (n) encountered in a dataset, and is therefore given by $1/\sqrt{n}$.

Discussion

Discussion: Mass Spectra & Charge-State-Ratios

The presence of the $(Mo_2)^{2+}$ dimer ions between *m/z* = 92 – 100 Da in the mass spectra during laser pulsing at the higher laser pulse energy is indicative of field-evaporation at a higher temperature relative to the lower laser pulse energy, Figure 2(e). Thermally induced surface diffusion may also be promoted due to the higher temperatures of the nanotip's surface achieved with the higher laser pulse energies. Surface diffusion reduces the spatial resolution in the 3-D APT reconstruction through a smearing or blurring effect [36].

As previously mentioned, the creation of complex molecular ions during field-evaporation at higher laser pulse energies may go entirely unnoticed by the user. In the case of Ti alloys with a Mo addition, the probability of complex molecular ion formation can be minimized during experimentation by decreasing the laser pulse energy. This decreases the surface temperature at the time of field-evaporation, thereby minimizing $(Mo_2)^{2+}$ and $(Mo_2)^{3+}$ formation. This should also limit the formation of complex molecular ions associated with TiH and TiO, which also depend on the partial pressures of H_2 and O_2 in the vacuum system. They are furthermore associated with the surface diffusivities of interstitial atoms [37]. The presence of (TiH)+ can be readily identified in Mo containing Ti alloys by the peak at 51 Da.

Although the physical chemistry of gas-metal reactions in a high electric field is a complex topic and not the focus of this article, it is noted in the current work that metal-hydrides and oxides are formed with titanium at higher laser pulse energies, Figure 2. The affinity of these elements for titanium is a well-known problem in titanium production. The high price of titanium production is a result of the high reactivity of oxygen with this metal. Similarly, the strong tendency of titanium to absorb hydrogen from air moisture (hydrogen pickup) is a major processing concern as it results in the well-documented material failures caused by hydrogen embrittlement [38].

The results herein are presented both in terms of the laser pulse energies of commercially available LEAP instruments manufactured by Cameca (Madison, WI USA), and the charge-state ratio (CSR) of Mo to (Mo + Mo_2) at *m/z* 46 and 92, respectively.

In the analysis of small precipitates and clusters in general, the measurements stepping the laser pulse energies (Figures 3 and 4) highlight the higher probability of collecting representative data at lower laser pulse energies. Other factors, such as sample geometry also influence the results. For this reason, charge state-ratios are a more reliable measure of the field evaporation conditions at the tip.

In the present study of Ti-5553 we find that minimizing both formation of molecular ions and dc-field evaporation can be achieved simultaneously with low laser pulse energies of approximately 10 pJ in the 5-8 kV range. This was performed while tracking the relative intensities of the peaks for different charge states or molecular cluster ions, specifically minimizing or eliminating $(Mo_2)^{2+}$ and $(TiH)^{+}$ molecular cluster ions. For the measurements performed at 10 pJ, the CSR is $^{46}Mo^{2+}$ / $^{92}(Mo^{+} + Mo_2^{2+})$ = 18.9 – 72.7 and the bulk Mo composition is in the range of 2.5 – 2.9 at.%, Table 2.

The lowest CSR = 2.4 is observed at the highest UV laser pulse energy applied of 50 pJ, and this measurement also gave the highest error in Mo composition, 4.5 at.% compared to the ICP-OES measurement of 2.4 at.%. The second measurement at 50 pJ gave a CSR = 5.0 and a Mo composition of 2.7 at.%. Similarly, a 30 pJ measurement with a CSR = 5.2 gave an acceptable Mo composition of 2.8 at.%, while the other 30 pJ measurement with a CSR = 3.8 gave a Mo composition of 3.2 at.%. In conclusion, the higher laser pulse energies of 30 –

50 pJ can result in significant isobaric peak overlap, with a CSR less than 5.0. This causes a large error in the determined Mo composition when this overlap is not deconvoluted. While deconvolution may improve the bulk composition calculated, it cannot correct for the inhomogeneity observed between the laser and shadow sides of the specimen, shown in Figure 5. Such issues are not encountered at the low laser pulse energy of 10 pJ.

From the 3-D reconstruction of the 2 h aged sample displayed in Figure 3a, the decrease of the CSR from 5.2 to 2.4 (Table 2) between 30 – 50pJ laser pulse energies, respectively, also caused analysis difficulties. While it is possible to calculate an average nanotip temperature over the evaporation duration, Marquis and Gault [39] clearly illustrated discrepancies in the determined tip temperature depending on the species used in the calculation. Thus, accurate nanotip temperature remains an area of on-going research.

Discussion: APT Reconstructions

The analysis issues arising from complex ion formation at higher laser pulse energies are most significant on the side of the APT nanotip facing the incident laser beam, Figure 4(a) – (c). Figure 4(a) displays the full 3-D reconstruction at different laser pulse energies, while Figure 4(b) and 4(c) show a 40 nm through-thickness slice at 30 pJ (CSR = 3.8) and 10 pJ (CSR = 19.9), respectively. The 3-D reconstructions illustrate clearly that the issues associated with complex molecular ion formation are inhomogeneous. It is certainly more difficult to discern the Ti-rich ω-precipitates on the laser side of the nanotip, Figure 4. The effect of the higher laser pulse energy on the detected ω volume fraction is apparent visually with the applied Ti-rich isoconcentration surface values in Figure 3(a) and 4. There is a clear depletion of the precipitates in the regions with significant formation of complex molecular ions at the higher energies, Figures 3(a) and 4.

Discussion: Proximity Histogram Concentration Profiles (Proxigrams)

If the elemental ion peaks in the mass spectrum are not deconvoluted from the overlapping complex molecular ion peaks, which arise at high laser pulse energies then the resultant bulk composition is too rich in the Mo concentration (bold font, Table 2). There are similar discrepancies observed in the proxigrams generated from the higher laser pulse energy data. Proxigrams were generated for the 30, 40 and 50 pJ laser pulse energy data using a Ti-rich isoconcentration surface value (86 at.%) for the 2 h aged sample, shown as a supplementary figure. From these proxigrams, the apparent concentration of Mo in the matrix increases with laser pulse energy, with a corresponding decrease of the Ti concentration.

The proximity histogram concentration profiles for the 300 °C/1 h and 300 °C/8 h aging-treatments are displayed in Figure 6, which are created using the 85 at.% Ti isoconcentration surface values. The ω-phase is Ti-rich relative to the β-matrix, and depleted in all solute additions. The ω/β interface is rich in oxygen (O) after just a 1 h aging-treatment. The interfacial region becomes richer in Al between the 1 and 8 h aging-treatments. This is notable, as O and Al are strong α-stabilisers. Thus, this interfacial enrichment of Al and O may play a role in the subsequent formation of the stable α-phase

by lowering the nucleation barrier. This hypothesis is strengthened by recent high-angle annular dark-field high-resolution scanning transmission electron microscopy (HAADF-HRSTEM) results displaying α-laths between ω-precipitates and the β-matrix, which are in contact with the ω-interface [13,14].

Discussion: Precipitate Nucleation and Growth

The spread in results in Figures 7 (a) – (c) is associated with difficulties and statistical limitations arising from deconvoluting Ti containing complex molecular ions from the solute additions in overlapping peaks in the mass spectra. It highlights the difficulties in accurately deducing precipitate size, number density and volume fraction by atom-probe tomography. The Ti concentration determined by ICP-OES is 81.6 at.%, Table 2. The general trend in the data is that, when a constant Ti isoconcentration surface value is applied across all data-sets, a lower apparent Ti composition determined by APT (Table 2) results in a lower apparent precipitate volume fraction. For example, for the 2 h aging-treatment, the apparent Ti bulk concentration decreased from 80.4 to 78.6 at.% as the laser pulse energy was increased from 30 pJ (CSR=5.2) to 50 pJ (CSR=2.4) , Table 2. For this measurement, when an 85 at.% Ti isoconcentration surface value is utilized, the apparent higher concentration Ti sample (measured at 30 pJ) yields a higher apparent volume fraction. The same logic applies to the mean radius.

Although not displayed, an increase in the isoconcentration surface value from 85 to 87 at.% resulted in an order of magnitude decrease in the apparent precipitate number density when measured at high laser energies, specifically the 50 pJ (CSR = 2.4) laser pulsed energy data used of the 2 h aged sample.

From the number density value, there is extensive nucleation of the isothermal ω-phase during the first hour of aging (Figure 7b), presumably nucleating from the athermal ω-phase that is initially present. Following the first hour the number density achieves a plateau, while the volume fraction continues to increase slightly, Figures 7(a) and (b). The increase in volume fraction is associated with the continuous growth of the mean precipitate radius, Figure 7(c). Since the volume fraction is increasing through an aging time of at least 8 h, the nucleation and growth and transition to growth and coarsening regimes are observed, but certainly a quasi-steady-state coarsening regime is not acheived. Given that the alloy is quenched, the matrix may still be supersaturated after the initial nucleation regime in the first hour of aging, leading to the simultaneous increase of the volume fraction and mean radius.

Discussion: Comparison to Archival Literature

The first APT analysis of Ti-5553 alloys was reported in 2009 utilizing the voltage mode, with a pulse voltage that was 30% of the steady-state applied dc voltage [18]. In that research, the isothermal ω-phase was identified by rather small compositional fluctuations, and the measured Ti bulk composition appears to be smaller than anticipated. The same authors note elsewhere that in general large pulse fractions should be avoided when measuring Ti-5553 [40]. The lower dc-fields can lead to adsorption of residual gases and result in field corrosion, and therefore the possibility of effects on the measured

concentrations cannot be ruled out. Thus, although the artifacts induced by large pulse fractions may be different to those induced by large laser pulse energies, there were initial concerns regarding the experimental methodology when studying Ti-5553 by APT using voltage pulsing.

More recently, the isothermal ω-phase in Ti-5553 was measured at a lower pulsing voltage, 20 % of the steady-state applied dc voltage [16]. By employing proximity histogram concentration profiles, the authors reported an ω-phase phase enriched in Ti and depleted in all solute additions [16]. This is in agreement with the results presented in this current article. Their samples had been prepared by isochronal heating with a 5 °C/ min rate to 350 °C, followed by rapid cooling.

The isothermal ω–precipitates of Ti-5553 observed herein are Ti-enriched and also depleted in all solute elements (Mo, Cr, Al, V and Fe) after aging for more than 1 h at 300 °C. The nucleation mechanism of athermal ω-precipitates that form on quenching from a solutionizing temperature in the beta-phase field [11] is currently being debated. Although not shown, a concentration frequency distribution analysis was applied to the quenched (0 h aging) Ti-5553 alloy and it revealed no evidence that athermal ω forms with a compositional change. This is in agreement with the results of a SANS study of Ti-5553, which suggests that there is very little compositional contrast, if any, of athermal ω with the β-matrix in these alloys [11].

The APT results reported for a Ti-6554 [14,15,17] alloy differ dramatically to the results presented herein for Ti-5553. In their work on Ti-6554, these authors discuss the formation of ω-embryos for aging times between 0 - 12 h at 300 °C. These embryos are depleted solely in Mo, and the concentration of all the other solute additions (Cr, V, Al) within the precipitates is approximately equal to their bulk concentrations. Thus, the embryos must also be enriched in Ti. At aging times longer than 12 h of Ti-6554, they observed that the isothermal ω–precipitates are depleted in all solute elements [14]. Such embryos are not observed in the current study of Ti-5553 under the same heat-treatment conditions, but employing lower laser pulse energies. The Mo equivalence of Ti-5553 is ~ 8.1 wt.% and of Ti-6554 is ~14 wt.%, defined as the sum of the weighted averages of the elements present in the alloy and given by Mo_{eq} = Mo + 0.67V + 0.44W + 0.28Nb + 0.22Ta + 1.6Cr + 1.25Ni + 1.7Co + 2.9Fe − 1.0Al (wt.%) [41]. Thus, a difference in precipitation pathways or kinetics may be due to this difference in composition of Ti-5553 and Ti-6554. It is difficult to state this conclusively, as the earlier APT analyses of Ti-6554 [14,17] were performed with laser pulse energies between 70 - 80 pJ, which is higher than those illustrated to cause data analysis difficulties in our research.

Discussion: Discrepancies in the Experimental Data

It is not fully understood as to why the LEAP5000X S identified the Ti rich ω-precipitates after a 1 h aging treatment at 300 °C, while the measurement performed on the LEAP4000X Si did not. The nanotips were produced from the same lift-out procedure (i.e., the APT specimens were produced from within 20 μm of each other within the same grain), and the isothermal ω-phase nucleates homogeneously [8,9]. The difference in charge state ratios of the 1 h aged samples presented in Table 2 may be significant. They indicate that the sample measured using the LEAP4000X Si had an average higher effective nanotip

temperature at the time of field-evaporation than that measured by the LEAP5000X S. A hypothesis is that the improved counting statistics provided by the higher detection efficiency of the LEAP 5000 XS *may* partially compensate for a loss of clear distinction when trying to delineate between phases with a small compositional amplitude or difference in composition.

Discussion: Correlation to Mechanical Properties

The increase in Ti-5553 hardness after a 300 ^{o}C/1 h aging treatment (Figure 1b) is consistent with early stage nucleation of high number density isothermal ω precipitates (Figure 7b). This phase is enriched in Ti and depleted in all solute additions (Figure 6). A variation of ω, which is solely enriched in Ti and depleted in Mo, was not observed. With the LEAP5000X S APT and accounting for the sensitivity of materials characterization to instrument parameters, it is possible to correlate directly nanoprecipitates to mechanical properties at early nucleation times, rather than back-extrapolating the correlation from longer aged samples.

Summary and Conclusions

- It has been shown that higher laser pulse energies should be avoided when studying nanoscale precipitation in Ti-alloys. This is due to an associated high surface temperature at the time of field evaporation, which favors the formation of complex molecular ions. The associated mass spectral peak overlaps inherently complicates data analysis. It is critical to minimize these overlaps to enable accurate quantification and detection of nanoscale precipitates, even if they are highly concentrated like the ω–precipitate results presented in this article. The results are discussed both in terms of laser pulse energies and charge-state ratios. It also appears from the archival literature that high pulse-fractions in the voltage pulsing mode should also be avoided [13,40].
- We note that a measurement performed on a LEAP5000 XS detected early precipitation in Ti-5553 after a 1 h aging treatment at 300 ^{o}C. These precipitates were not observed in a measurement performed on a LEAP 4000X Si in a separate APT specimen from the same grain.
- There is no indication from our APT analyses that athermal ω–precipitates form in Mo depleted zones in Ti-5553, in agreement with previously reported small-angle neutron-scattering (SANS) data [9].
- After a 300 °C/1 h aging-treatment Ti-rich/solute-depleted isothermal ω–precipitates are observed, with oxygen enrichment at the ω-precipitate/β-matrix interface. After an 8 h aging-treatment, the interface is enriched with Al relative to the 1 h aging-treatment, in addition to the O enrichment. Both Al and O are α-phase stabilizers and it is suggested that the isothermal ω/β interface serves as an α nucleation site due to a reduced nucleation barrier. This is a reasonable hypothesis, based on recently published high-angle annular dark-field-high resolution scanning transmission electron microscopy (HAADF-HRSTEM) results [13,14]. With the exception of the increase of the Al concentration at the interfacial region, there is little change in element partitioning between 1 - 8 h of aging.

- The isothermal ω-phase is in a nucleation regime for the first hour of aging at 300 °C, and nucleation and growth regimes that last for at least 8 h. There is a rapid increase in number density in the first hour, followed by a plateau. The isothermal ω-phase volume fraction and mean radius continue to increase throughout the 8 h aging-treatment.

Acknowledgments
JC acknowledges support from the European Union Seventh Framework Programme under the Marie Curie grant agreement number 628643. Atom-probe tomography measurements were performed at the Northwestern University Center for Atom-Probe Tomography (NUCAPT) and the LEAP tomograph was purchased and upgraded with funding from the NSF-MRI (DMR 0420532) and ONR DURIP (N00014-0400798, N00014- 0610539, N00014-0910781) programs. NUCAPT received support from the MRSEC program (NSF DMR-1121262) at Northwestern's Materials Research Science and Engineering Center (MRSEC), the SHyNE Resource (NSF NNCI-1542205), and the Initiative for Sustainability and Energy (ISEN). The authors are grateful to DC Bell and AP Magyar at Harvard University for the APT measurements performed on their LEAP 4000X HR.

References

1. Radecka A., Bagot PAJ., Martin TL., Coakley J., Vorontsov VA., Moody MP, Ishii H., Rugg D., Dye D. (2016). The formation of ordered clusters in Ti-7Al and Ti-6Al-4V. *Acta Mater* **112**, 141 – 149.
2. Radecka A., Coakley J., Vorontsov VA., Martin TL,. Bagot PAJ., Moody MP., Rugg D., Dye D. (2016). Precipitation of the ordered α_2 phase in a near-α titanium alloy. *Scr Mater* **117**, 81 – 85.
3. Rosenberg HW. (1970). Titanium Alloying in Theory and Practise. In *The Science, Technology and Application of Titanium*, Jaffee RI & Promisel NE (Eds.) p. 851 – 859. Pergamon Press, London, UK.
4. Neeraj T., Hou D., Daehn G.,Mills M. (2000). Phenomenological and microstructural analysis of room temperature creep in titanium alloys, *Acta Mater* **48**, 1225 - 1238.
5. Leyens C. & Peters M. (Eds.). (2003). *Titanium and Titanium Alloys: Fundamentals and Applications*, Wiley-VCH Verlag GmbH & Co. KGaA, Weinheim, FRG.
6. Lütjering G. & Weissman S. (1970). Mechanical properties of age-hardened titanium-aluminum alloys, *Acta Metall*. **18** 785 – 795.
7. Jones NG., Dashwood RJ., Dye D., Jackson M. (2008) Thermomechanical Processing of Ti-5Al-5Mo-5V-3Cr. *Mater Sci & Eng A* **490**, 369 – 377.
8. Coakley J., Vorontsov VA., Littrell KC., Heenan RK., Ohnuma M., Jones NG., Dye D. (2015). Nanoprecipitation in a Beta-Titanium Alloy. *J Alloys Comp.* **623**, 146 – 156.
9. Coakley J., Vorontsov VA., Jones NG., Radecka A., Bagot PAJ., Littrell KC., Heenan RK., Hu F., Magyar AP., Bell DC ,Dye D. (2015). Precipitation Processes in the Beta-Titanium Alloy Ti-5Al-5Mo-3Cr. *J Alloys Comp.* **646**, 946 – 953.
10. Coakley J., Rahman KM., Vorontsov VA., Ohnuma M., Dye D. (2016). Effect of Precipitation on Mechanical Properties in the β-Ti alloy Ti-24Nb-4Zr-8Sn. *Mater Sci & Eng A* **655**, 399 – 407.

11. Coakley J., Radecka A., Dye D., Bagot P.A.J., Stone HJ., Seidman D.N., Isheim D. (2016). Isothermal omega formation and evolution in the Beta-Ti alloy Ti-5Al-5Mo-5V-3Cr. *Phil Mag Letters* **96**(11), 416-424.
12. Coakley J., Isheim D., Radecka A., Dye D., Stone HJ., Seidman DN. (2016). Microstructural evolution in a superelastic metastable beta-Ti alloy. *Scripta Mater.* **128**, 87–90.
13. Zheng Y., Williams REA., Wang D., Shi R., Nag S., Kami P., Sosa JM., Banerjee R., Wang Y., Fraser HL. (2016). Role of ω phase in the formation of extremely refined intragranular α precipitates in metastable β-titanium alloys. *Acta Mater* **103**, 850 – 858.
14. Li T., Kent D., Sha G., Stephenson LT., Ceguerra AV., Ringer SP., Dargusch MS., Cairney JM. (2016). New insights into the phase transformations to isothermal ω and ω-assisted α in near β-Ti alloys. *Acta Mater* **106**, 353-366.
15. Li T., Kent D., Sha G., Dargusch MS., Cairney JM. (2015). The mechanism of ω assisted α phase formation in near β-Ti alloys. *Scri Mater* **104**, 75 – 78.
16. Zheng Y., Williams REA., Sosa JM., Alam T, Wang Y., Banerjee R., Fraser HL. (2016). The indirect influence of the ω phase on the degree of refinement of distributions of the α phase in metastable β-Titanium alloys. *Acta Mater* **103**, 165 – 173.
17. Li T., Kent D., Sha G., Cairney JM., Dargusch MS. (2016). The role of ω in the precipitation of α in near-β Ti alloys. *Scri Mater* **117**, 92 – 95.
18. Nag S., Banerjee R., Srinivasan R., Hwang JY., Harper M., Fraser HL. (2009). ω-assisted nucleation and growth of α precipitates in the Ti-5Al-5Mo-5V-3Cr-0.5Fe β titanium alloy. *Acta Mater* **106**, 353 – 366.
19. Jones NG., Dashwood RJ., Jackson M., Dye D. (2009). β phase decomposition in Ti-5Al-5Mo-5V-3Cr. *Acta Mater* **57**, 3830 – 3839.
20. Thompson K, Lawrence D, Larson DJ, Olson JD, Kelly TF, Gorman, B (2007). In situ site-specific specimen preparation for atom probe tomography. Ultramicroscopy **107**, 131-139.
21. Kelly TF. & Larson DJ. (2000). Local electrode atom probes. *Mater Char* **44**, 59 – 85.
22. Larson DJ., Prosa TJ., Ulfig RM., Geiser BP., Kelly TF., (2013). *Local Electrode Atom Probe Tomography: A User's Guide*. p. 61. Springer, New York, USA.
23. Prosa TJ., Geiser BP., Lawrence D., Olson D., Larson DJ. (2014). *Developing detection efficiency standards for atom probe tomography*, SPIE Proceedings. 9173 (917307). doi:10.1117/12.2062211.
24. Gault B., Moody MP., Cairney JM., Ringer SP. (2012). *Atom Probe Microscopy.* p. 242. Springer, New York, USA.
25. Rüsing J., Sebastian JT., Hellman OC., Seidman DN. (2000). Three-dimensional Investigation of Ceramic/Metal Heterophase Interfaces by Atom-probe Microscopy. *Microsc. Microanal*. **6**, 445–451.
26. Hellman OC., Vandenbroucke, JA., Rüsing J., Isheim D., and Seidman DN. (2000). Analysis of Three-Dimensional Atom-Probe Data by the Proximity Histogram. *Microsc. Microanal.* Vol. **6**, 437 - 444.
27. Hellman OC., Rüsing J., Sebastian JT., Seidman DN. (2001). Atom-by-atom chemistry of internal interfaces: simulations and experiments. *Mater. Sci .Eng. C*. **15**, 13–15.

28. Hellman OC., Vandenbroucke J., Blatz du Rivage J., Seidman DN. (2002). Application software for data analysis for three-dimensional atom probe microscopy. *Mater. Sci. Eng. A.* **327**(1), 29–33.
29. Hellman OC., Blatz du Rivage J., Seidman DN., (2003). Efficient sampling for three-dimensional atom probe microscopy data. *Ultramicroscopy.* **95**, 199–205.
30. Isheim D., Hellman OC., Rüsing J., Seidman DN. (2002). Atomic-Scale Structure and Chemistry of Segregation at Matrix/Precipitate Heterophase Interfaces*. Interf. Sci*. **9**. 257–264.
31. Tsong TT. (1986). Observation of doubly charged diatomic cluster ions of a metal. *J. Chem. Phys.* 85, 639.
32. Tsong TT. (1990), *Atom-Probe Field-Ion Microscopy*, p. 63. Cambridge University Press, Cambridge, UK.
33. Isheim D., Seidman, DN., and Wanderka, N., (2007). Doubly- and Triply-Charged Diatomic Molybdenum Cluster Ions As Observed in Pulsed-Laser Assisted Local-Electrode Atom-Probe (LEAP™) Tomography. *Proceedings of the Microscopy & Microanalysis 2007 Conference*, August 5-9, Ft. Lauderdale, Florida; *Microscopy and Microanalysis*, **13** (Suppl. 2), (2007) 1650CD-1651CD.
34. Böhlke, JK., de Laeter JR., De Bièvre, P., Hidaka, H., Peiser HS., Rosman KJR., Taylor PDP. (2001). Isotopic Compositions of the Elements. *J. Phys. Chem. Ref. Data*. **34**, 57 - 67.
35. Chebotareva ES. & Nuzhdina SG. (1973). Observation of omega-titanium in a composite hard facing alloy based on fine-grain diamonds. *Fizika Metallov i Metallovedenie* **36**, 200 – 202.
36. Gault B., Danoix F., Hoummada K., Mangelinck D., Leitner H. (2012). Impact of directional walk on atom probe microanalysis. *Ultramicroscopy*. **113**, 182–191.
37. Kim YJ., Seidman DN. (2015). Atom Probe Tomographic Analyses of Hydrogen Interstitial Atoms in Ultrahigh Purity Niobium. *Microsc Microanal* **21**, 535-543.
38. Lütjering G. & Williams J.C. (2007) *Titanium*, p. 108. Springer-Verlag, Berlin.
39. Marquis E., Gault B. (2008) Determination of the tip temperature in laser assisted atom-probe tomography using charge state distributions. *Journal of Applied Physics* **104**, 084914.
40. Nag S., Banerjee R., Hwang JY., Harper M., Fraser HL. (2009). Elemental partitioning between α and β phases in the Ti–5Al–5Mo–5V–3Cr–0.5Fe (Ti-5553) alloy. *Phil Mag* **89**:6, 535-552
41. Weiss I., Semiatin S.L., Thermomechanical processing of beta titanium alloys—an overview. *Mater. Sci & Eng A* **243**: 46-65.

Table and Figure Captions

LEAP Instrument	Laser λ (nm)	Ion Detection Efficiency (%)	Laser Energy (pJ)	Stage Temp. (K)	Aging Time (h)	Ion Counts (M)	Precipitates Identified
3000X HR	532*	38	200*	40	8	52	Y
4000X HR	355	38	50	44	8	57	Y
4000X Si	355	58	30 - 10	30	8	48	Y
4000X Si	355	58	10	30	4	82	Y
4000X Si	355	58	30 - 50	45	2	78	Y
4000X Si	355	58	10	30	1	29	N
5000X S	355	77	10	30	1	56	Y
4000X Si	355	58	10	30	0	53	N
5000 XS	355	77	10	30	0	14	N

Table 1. Test matrix of the four different types of LEAP instruments used in this study of isothermal ω-precipitation in Ti-5553 alloys, aged for 0 - 8 h at 300 °C. The green laser is identified with an asterix*. All other tomographs are equipped with a UV laser. The laser pulse energies and specimen stage temperatures used for each measurement are listed along with the specific tomograph, ion detection efficiency, total ion counts of each measurement run in millions (M) detected, and whether precipitates were identified by APT (Y) or not (N).

Instrument	Laser Energy (pJ)	$^{46}Mo^{2+}/^{92}(Mo^{+}+Mo_2^{2+})$	Aging Time (h)	Ion Counts (M)	Ti	V	Fe	Al	Mo	Cr	O
ICP-OES	-	-	-	-	81.6	4.6	0.3	8.2	2.4	2.6	0.4
3000X HR	200*	9.8	8	48	79.9	5.1	0.3	8.3	2.9	2.9	0.5
4000X HR	50	5.0	8	52	80.6	4.9	0.2	8.3	2.7	2.9	0.4
4000X Si	*10*	19.9	8	8	79.9	5.1	0.3	8.5	2.8	2.8	0.5
4000X Si	*30*	3.8	8	19	80.4	4.7	0.2	8.2	3.2	2.8	0.5
4000X Si	10	72.7	4	54	80.1	5.2	0.2	8.4	2.7	2.8	0.5
4000X Si	*30*	5.2	2	13	80.4	4.9	0.2	8.4	**2.8**	2.7	0.6
4000X Si	*40*	3.2	2	16	80.0	4.8	0.2	8.4	**3.2**	2.8	0.5
4000X Si	*50*	2.4	2	13	78.6	4.7	0.2	8.4	**4.5**	2.9	0.5
4000X Si	10	18.9	1	21	79.6	5.4	0.3	8.6	2.5	2.9	0.5
5000X S	10	39.9	1	46	79.0	5.5	0.4	8.6	2.9	3.1	0.5
4000X Si	10	39.6	0	52	80.3	5.2	0.3	8.3	2.5	2.9	0.5
5000X S	10	63.1	0	11	79.4	5.1	0.3	9.3	2.6	2.7	0.6

Table 2. Bulk compositions in atomic % of the Ti-5553 alloy, determined by inductively coupled plasma optical emission spectrometry (ICP-OES) [7] and by different atom probe tomography LEAP instruments, aged for 0 - 8 h at 300 °C. The green laser is identified with an asterix*. All other tomographs are equipped with a UV laser. The laser pulse energies for each measurement are listed along with the total ion counts used in each data reconstruction in millions (M) detected. The intensity ratio during field evaporation of Mo to (Mo + Mo_2) at *m/z* 46 and 92, respectively, are shown. Measurements where the laser pulse energy was changed during the data acquisition are highlighted in the first two columns by italic font. The effect of high laser pulse energy on apparent Mo composition is highlighted in bold font. Further experimental parameters are provided in Table 1.

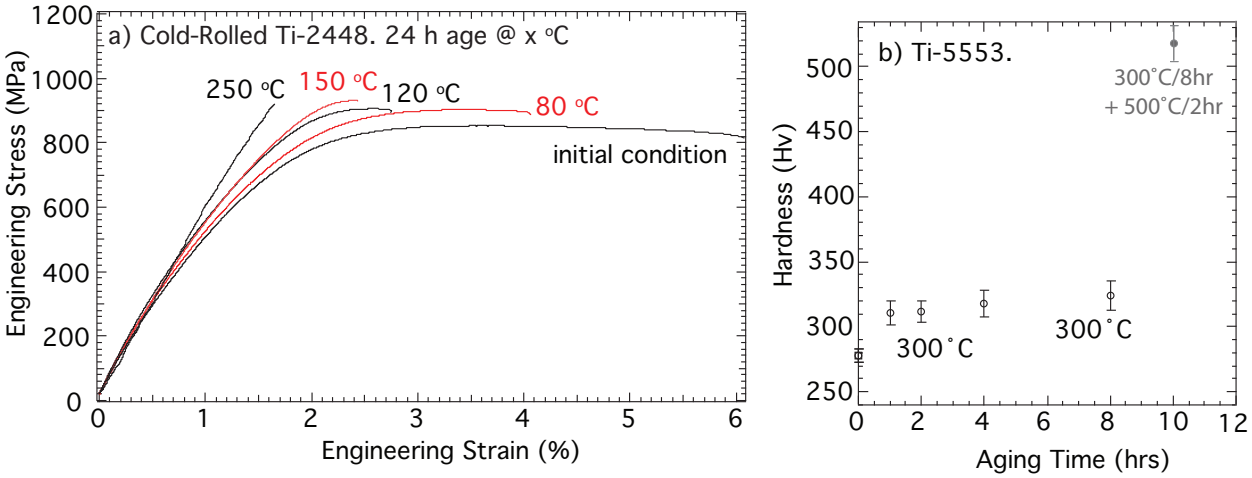

Figure 1. a) Effect of low temperature aging between 80 – 250 °C for 24 h on room-temperature tensile properties of cold rolled metastable β-Ti alloy Ti-2448 (Ti-24Nb-4Zr-8Sn wt.%) [10]. b) Effect of low temperature aging on room-temperature hardness of Ti-5553 (Ti-5Al-5Mo-5V-3Cr wt.%). Samples were aged at 300 °C for up to 8 h, and a dual heat-treatment sample of 300 °C/8 h + 500 °C /2 h was also performed [9]. Images reproduced with the permission of the publisher.

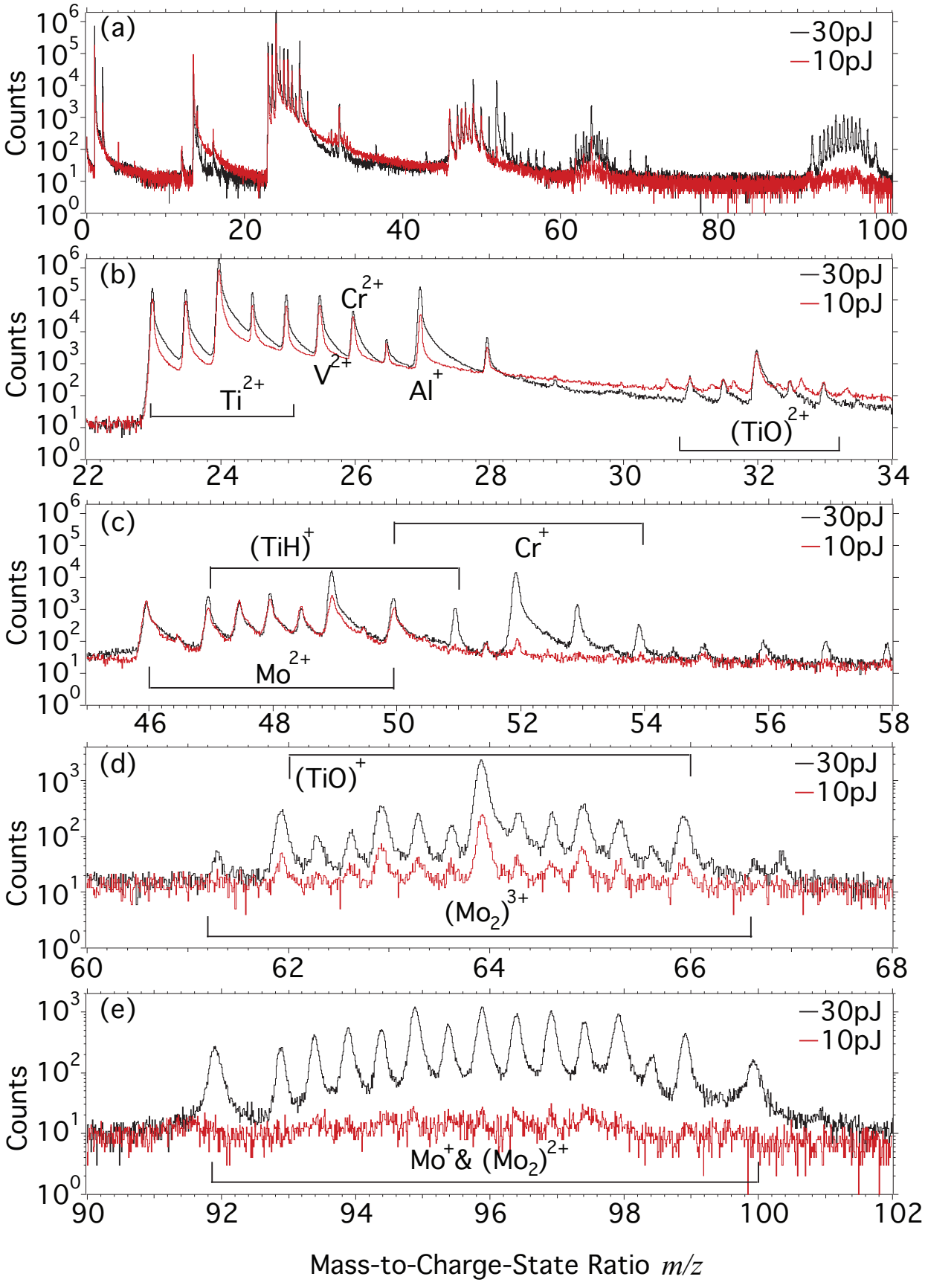
(a)
—30pJ
—10pJ
Counts
(b)
Cr2+
V2+
Ti2+
Al+
(TiO)2+
(c)
(TiH)+
Cr+
Mo2+
(d)
(TiO)+
(Mo2)3+
(e)
Mo+ & (Mo2)2+
Mass-to-Charge-State Ratio m/z

Figure 2. APT mass spectra of Ti-5553 aged for 8 h at 300 °C obtained with 10 or 30 pJ laser pulse energies utilizing a LEAP 4000X Si atom-probe tomograph. (a) Displays the complete spectrum and (b) – (e) are magnified sections to highlight the isotopic distributions of individual ions or molecular ions.

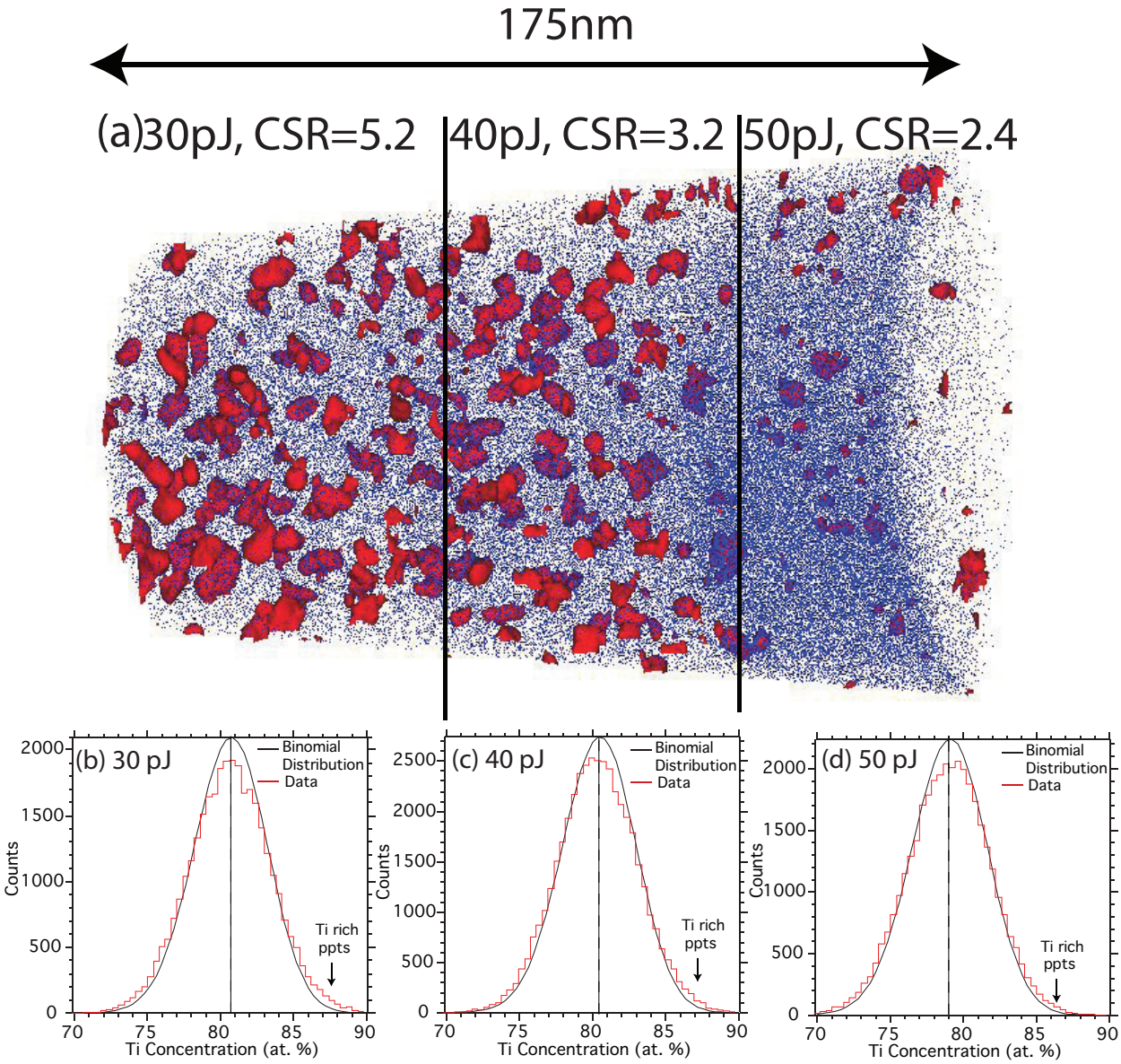

Figure 3. (a) APT reconstruction of Ti-5553 aged for 2 h at 300 °C. Data obtained with the UV laser pulse energy stepped from 30 to 40 and 50 pJ after ~15 million ions collected, respectively, utilizing a LEAP 4000X Si atom-probe tomograph. The charge-state ratio (CSR) of Mo to (Mo + Mo_2) at *m/z* 46 and 92, respectively, are also given. To highlight the Ti-rich precipitates (ppts), an 86 at.% Ti isoconcentration surface is superposed in red. For clarity, only 15 % of the Mo ions are displayed (blue dots). (b) – (d) Ti concentration frequency distributions, red, for sections with the different laser energies, 30 pJ in (b), 40 pJ in (c), and 50 pJ in (d), respectively, for the same dataset, calculated with a block size of 250 atoms. A dashed line highlights the mean value. Binomial distributions are shown as black

lines for comparison with the experimental data. The Ti-rich tails, representing Ti-rich precipitates, are most pronounced at lower laser pulse energies (arrows in (b) - (d)).

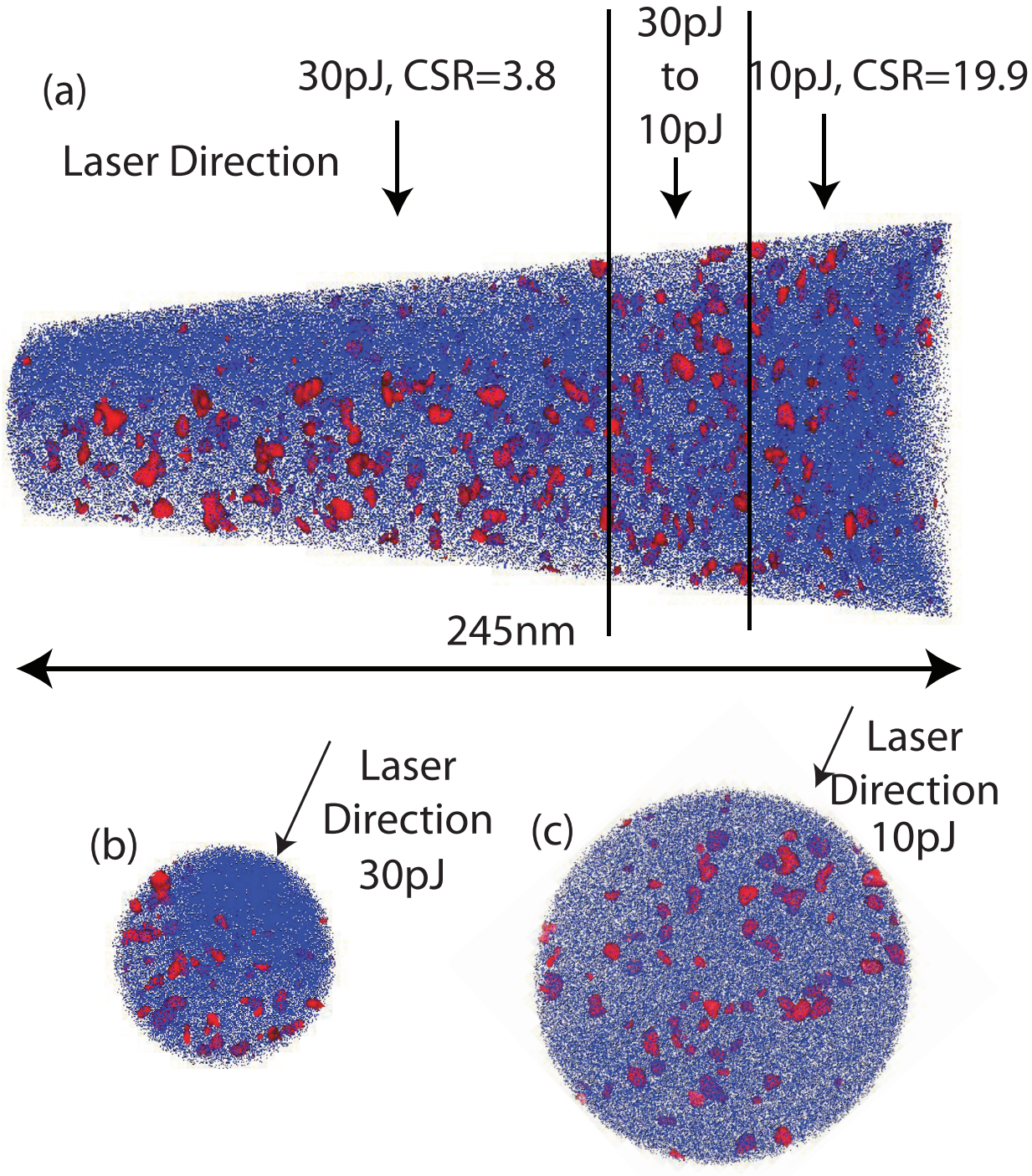

Figure 4. (a) APT reconstruction of Ti-5553 aged for 8 h at 300 °C. Data obtained with the UV laser pulse energy stepped from 30 pJ to 10 pJ after ~19 million ions collected, utilizing a LEAP 4000X Si tomograph. The charge-state ratio (CSR) of Mo to (Mo + Mo_2) at *m/z* 46 and 92, respectively, are given. To highlight the Ti-rich precipitates, an 88 at.% Ti-rich

isoconcentration surface is superposed in red. For clarity, only 35 % of the Mo ions are shown (blue dots). (b) - (c) View through 40 nm thickness of the APT reconstruction with Ti-rich precipitates again highlighted with an 88 at.% Ti-rich isoconcentration surface superposed in red and with 75 % Mo ions shown (blue dots), for 30 and 10 pJ laser pulse energies, respectively. All sub-figures are to the same scale, and highlight the incident laser direction.

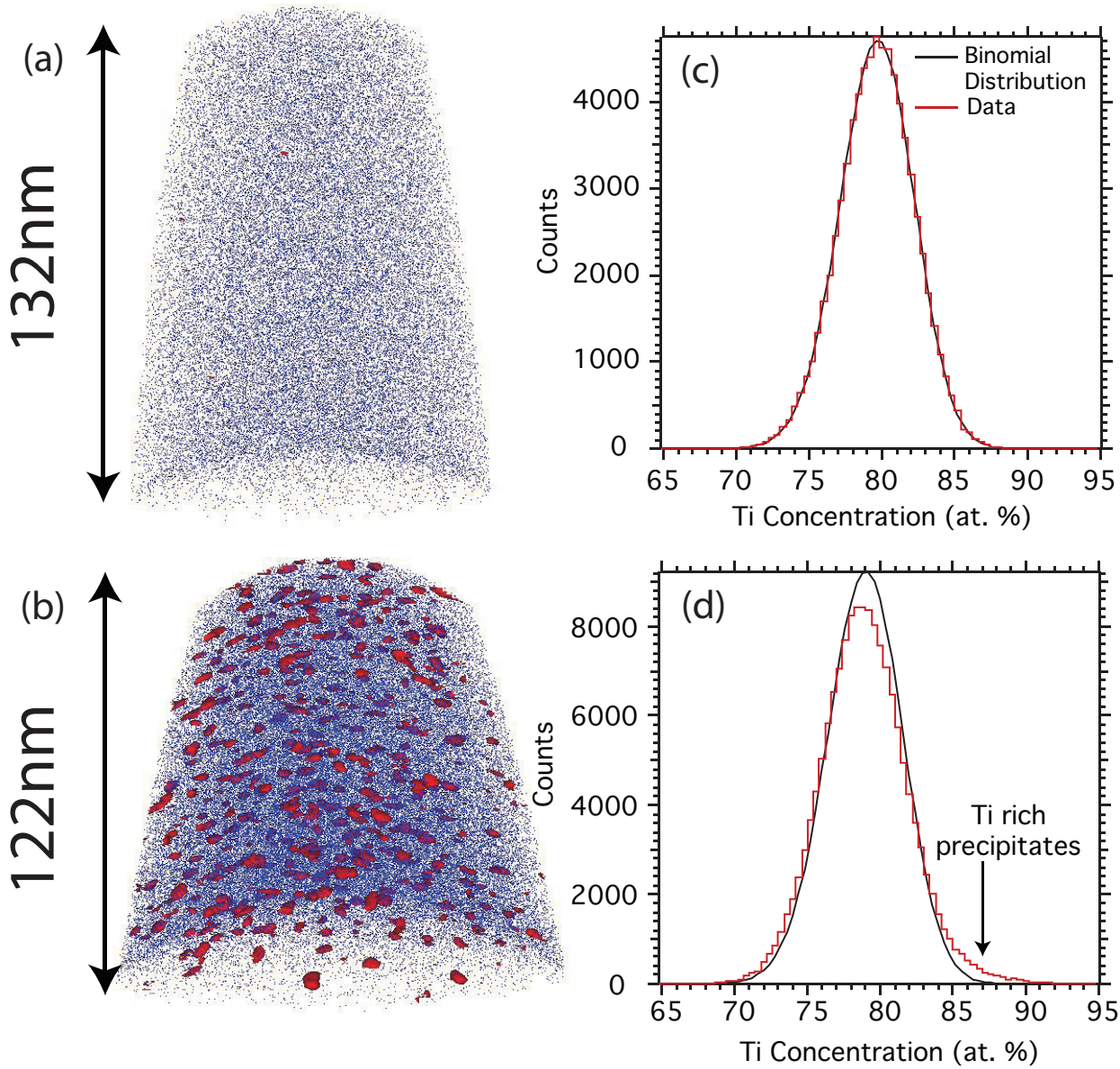

Figure 5. APT reconstructions of Ti-5553 aged for 1 h at 300 °C obtained with (a) a LEAP 4000X Si atom-probe tomograph, and (b) a LEAP 5000 XS. An 85 at.% Ti isoconcentration surface is superposed (red). 10 % of the Mo ions detected (blue dots) are displayed to outline the shape of the reconstruction. (c) Corresponding Ti concentration frequency distributions (stepped red line) constructed with block sizes of 250 atoms for the LEAP 4000X Si data, and (d) the LEAP 5000 XS data, respectively. The binomial distributions are displayed as black lines for comparison with the experimental data.

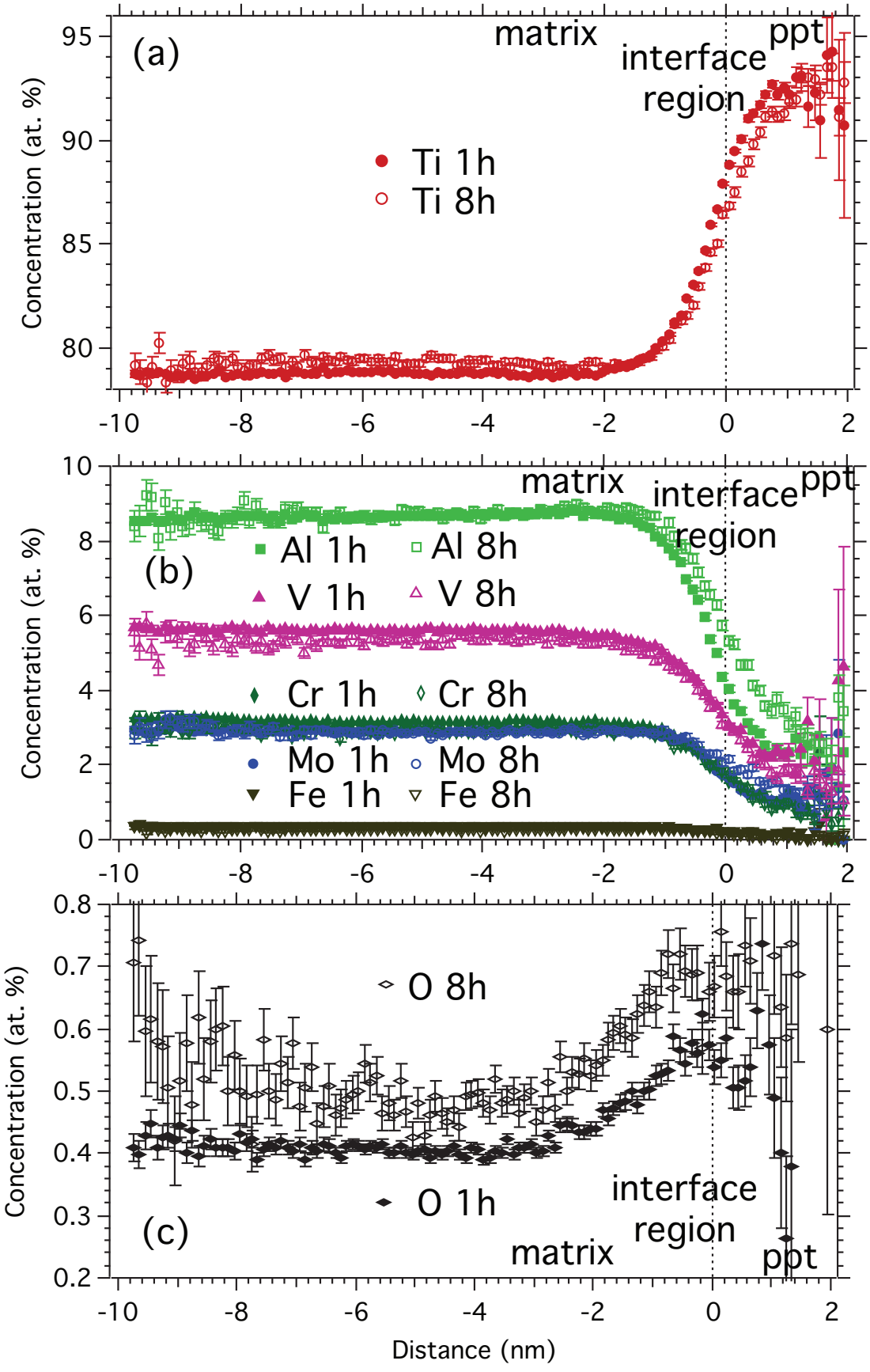
(a)
matrix
interface region
ppt
Ti 1h
Ti 8h
Concentration (at. %)
(b)
Al 1h
Al 8h
V 1h
V 8h
Cr 1h
Cr 8h
Mo 1h
Mo 8h
Fe 1h
Fe 8h
(c)
O 8h
O 1h
Distance (nm)

Figure 6. (a) – (c) Proximity histogram concentration profiles of Ti-rich precipitates with respect to an 85 at.% Ti isoconcentration surface, for Ti-5553 aged for 1 or 8 h at 300 °C. The approximate inflection points of the Ti profiles are highlighted with a dashed line, as an approximation for the center of the interfacial region between the matrix and precipitate. The larger error range in the oxygen concentration deduced in the 8 h data compared to the 1 h data is associated with the poorer counting statistics, where the 8h profile is formed from 8 million ions and the 1 h profile is formed from 46 million ions. The 1 h data was collected on the LEAP 5000X S, and the 8 h data was collected on the LEAP 4000X Si.

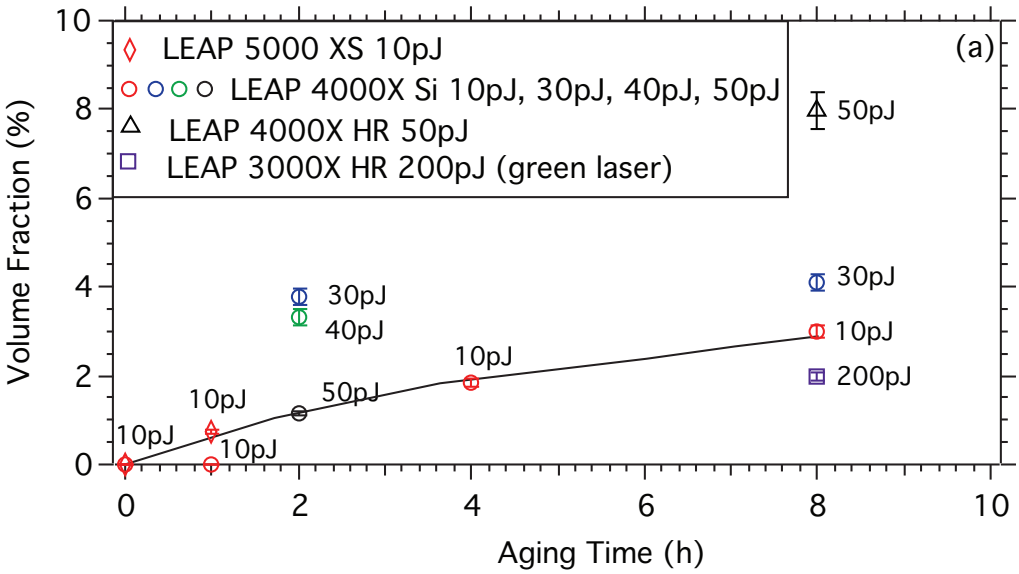
LEAP 5000 XS 10pJ
LEAP 4000X Si 10pJ, 30pJ, 40pJ, 50pJ
LEAP 4000X HR 50pJ
LEAP 3000X HR 200pJ (green laser)
(a)
Volume Fraction (%)
Aging Time (h)
10pJ
10pJ
10pJ
30pJ
40pJ
50pJ
10pJ
50pJ
30pJ
10pJ
200pJ

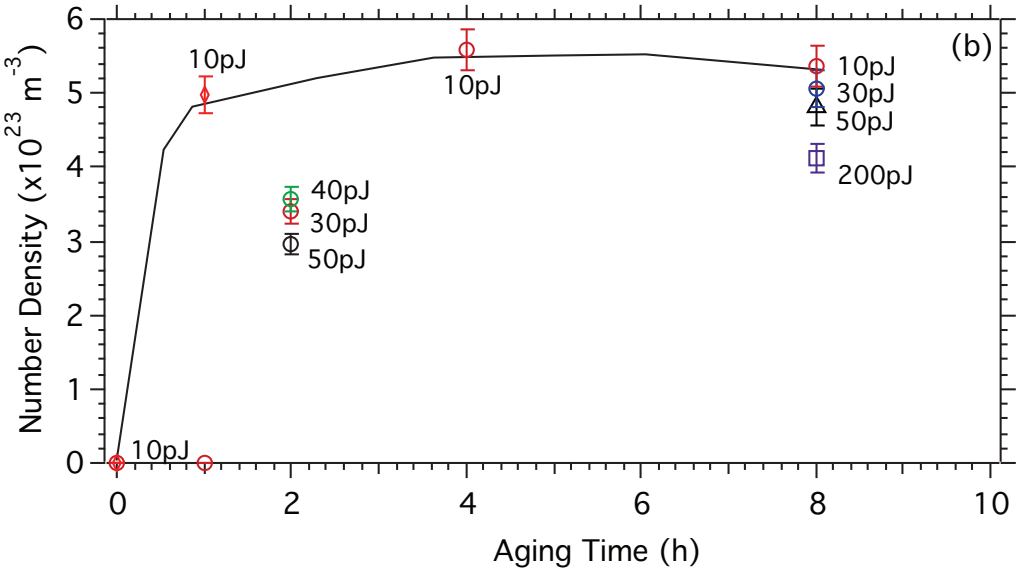
(b)
Number Density (x10^23 m^-3)
Aging Time (h)
10pJ
10pJ
10pJ
40pJ
30pJ
50pJ
10pJ
30pJ
50pJ
200pJ

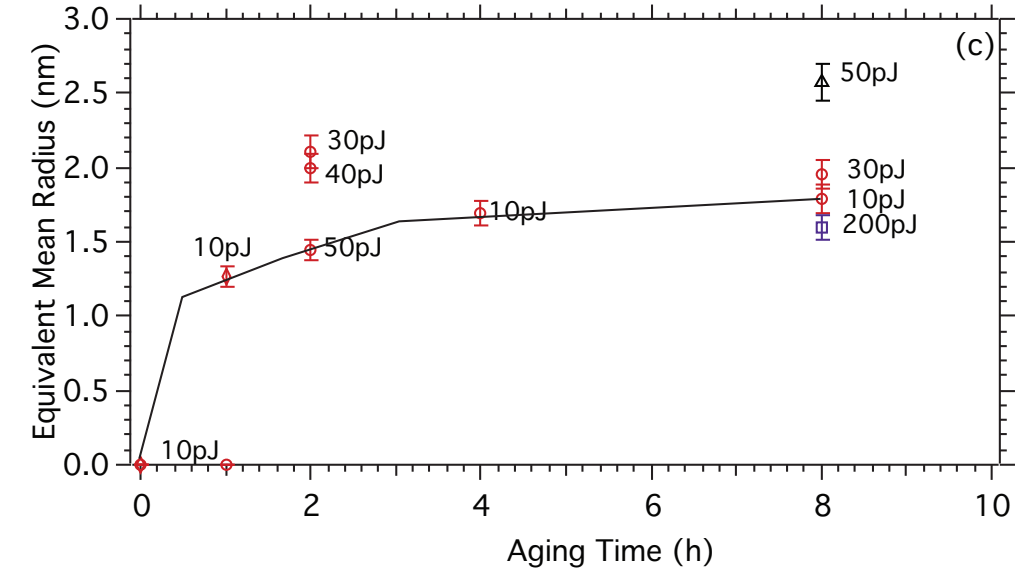
(c)
Equivalent Mean Radius (nm)
Aging Time (h)
10pJ
30pJ
40pJ
10pJ
10pJ
50pJ
50pJ
30pJ
10pJ
200pJ

Figure 7. (a) Measured volume fraction, (b) number density and (c) mean volume-equivalent radius of Ti-rich precipitates versus aging time in Ti-5553 aged for 0 - 8 h at 300 °C. The microstructural parameters are calculated from an applied 85 at.% Ti isoconcentration surface value. Guides to the eye, following the 10 pJ laser pulse energy data with highest charge-state ratio (CSR) of Mo to (Mo + Mo_2) at *m/z* 46 and 92, respectively, are included along with error bars of 5% error, approximated from the counting statistics of the number of precipitates encountered in the datasets.

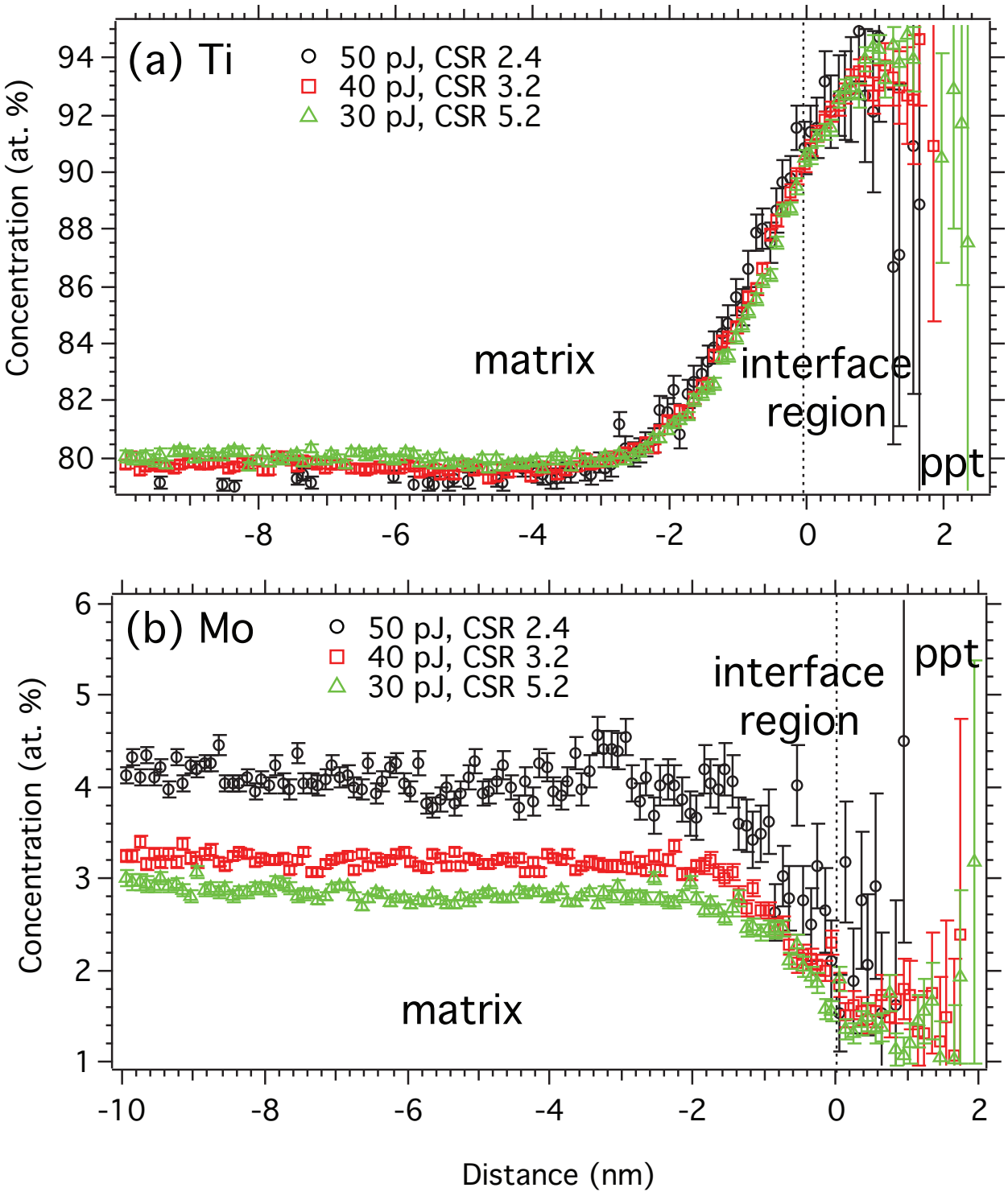

Supplementary Figure. a) Ti and b) Mo proximity histogram concentration profiles of Ti-rich precipitates with respect to an 86 at.% Ti isoconcentration surface, for Ti-5553 aged for 2 h at 300 °C. The approximate inflection points of the Ti profiles are highlighted with a dashed line, as an approximation for the center of the interfacial region between the matrix and precipitate. Data is presented in terms of the laser pulse energy applied for the measurement and the charge-state ratio (CSR) of Mo to (Mo + Mo_2) at *m/z* 46 and 92.